PAPER

Photoresponse improvement of mixed-dimensional 1D–2D GaAs photodetectors by incorporating constructive interface states†

Dengkui Wang,[a] Xue Chen,[a] Xuan Fang,[a] Jilong Tang, [iD] [a] Fengyuan Lin,[a] Xinwei Wang,[a] Guanlin Liu, [iD] [a] Lei Liao, [iD] *[b] Johnny C. Ho [iD] [c] and Zhipeng Wei [iD] *[a]

Mixed-dimensional optoelectronic devices bring new challenges and opportunities over the design of conventional low-dimensional devices. In this work, we develop unreported mixed-dimensional GaAs photodetectors by utilizing 1D GaAs nanowires (NWs) and 2D GaAs non-layered sheets (2DNLSs) as active device materials. The fabricated photodetector exhibits a responsivity of 677 A W^{-1} and a detectivity of 8.69×10^{12} cm Hz$^{0.5}$ W^{-1} under 532 nm irradiation, which are already much better than those of state-of-the-art low-dimensional GaAs photodetectors. It is found that this unique device structure is capable of converting the notoriously harmful surface states of NWs and 2DNLSs into their constructive interface states, which contribute to the formation of quasi-type-II band structures and electron wells in the device channel for the substantial performance enhancement. More importantly, these interface states are demonstrated to be insensitive to ambient environments, indicating the superior stability of the device. All these results evidently illustrate a simple but effective way to utilize the surface states of nanomaterials to achieve the high-performance photodetectors.

Introduction

In recent years, the development of 2D semiconductor materials has given birth to a new area of mixed-dimensional optoelectronic materials, including 3D–2D,[1] all-2D,[2–5] 1D–2D[6–9] and 0D–2D[10] heterostructures, which present new challenges and opportunities over conventional optoelectronics. Particularly, there have been many all-2D heterostructures developed by stacking different distinct 2D material layers on top of each other, providing various unique properties as summarized in several reviews.[11–13] Meanwhile, when traditional semiconductor materials are shrunk to the thickness of several

[a]State Key Laboratory of High Power Semiconductor Lasers, Changchun University of Science and Technology, Changchun 130022, China. E-mail: zpweicust@126.com
[b]State Key Laboratory for Chemo/Biosensing and Chemometrics, School of Physics and Electronics, Hunan University, Changsha 410082, China.
E-mail: liaolei@whu.edu.cn
[c]Department of Materials Science and Engineering, City University of Hong Kong, Hong Kong SAR 999077, China

†Electronic supplementary information (ESI) available: Detailed I_{ds}–V_{ds} of GaAs NWs and GaAs 2DNLSs with a series of illumination densities, the degree of surface bending of GaAs NWs or GaAs 2DNLSs, band structures of the mixed-dimensional GaAs photodetector, the responsivity of GaAs NW or GaAs 2DNLS photodetectors and the enlarged rise time and decay time curves. See DOI: 10.1039/d0nr06788a

atom layers, also known as 2D non-layered materials, they also exhibit many exceptional properties, such as strong electron confinement.[14–16] However, nanoscale materials (*e.g.* nanowires and 2D non-layered materials) have large surface-to-volume ratio with substantial amounts of surface dangling bonds and surface states that greatly hinder the optoelectronic performance of these materials.[17] Many efforts have then been devoted to eliminate these surface states for improving the material properties.[17,18] Surface passivation is one of the most common ways to minimize the surface states by removing the native oxide layers and saturating the dangling bonds on the material surface.[18,19] In fact, this surface state elimination may not necessarily be the best way to deal with the issues, because the surface after treatment would still be unstable, slowly reverting back to reform the surface states. Instead, it is of great significance to seek for a simple and reliable method to utilize these surface states in the material design for enhanced device performance.

Generally, as there are large amounts of surface states existing on the semiconductors, Fermi level pining would take place to lead to surface band bending.[17] This band bending promotes the spatial separation of holes and electrons there, which significantly enhances the separation efficiency of photo-generated carriers. Unfortunately, these photo-generated electrons are also largely trapped by these surface states, yield-

ing the poor responsivity and slower response speed of the subsequently fabricated devices.[20] Therefore, the surface states are widely considered as the adverse factors to deteriorate the device performance. On the other hand, there are several kinds of interface states associated with the semiconductor heterojunctions that can contribute to the device performance enhancement.[21–23] For instance, Tian *et al.* obtained a high gain in hybrid GaAs/graphene photodetectors by utilizing interface states, which act as hole-trapping centers to trap photo-excited holes.[23] In this regard, if the notoriously harmful surface states can be magically transformed into the constructive interface states, the optoelectronic properties of devices based on nanowires or 2D non-layered materials can be significantly improved.

Herein, we design and fabricate high-performance mixed-dimensional GaAs photodetectors by utilizing 1D GaAs nanowires (NWs) and 2D GaAs non-layered sheets (NLSs) as active materials. It is observed that the fabricated devices exhibit substantially enhanced performance due to the transformation of abundant detrimental surface states into constructive interface states. To be specific, the mixed-dimensional 1D–2D GaAs photodetectors can deliver a remarkable responsivity of 677 A W^{-1} at 25 V, which is several fold better than that of a GaAs NW photodetector and a GaAs thin film photodetector. Based on the detailed characterization, the notable enhancement of device photoresponsivity is predominantly attributed to the formation of a quasi-type II band structure, originating from the band bending caused by the surface states of 1D GaAs NWs and 2D GaAs NLSs. Moreover, the photo-generated electrons are found to accumulate at the interface among 1D transmission channels established by the interface states, in which the response speed of the fabricated photodetectors can be greatly improved. All these results can evidently indicate the utilization of surface states of 1D NWs and 2D NLSs to construct the favourable interface states as an effective strategy for the further performance enhancement of optoelectronic materials and devices.

Methods

Preparation of GaAs NWs

The GaAs NWs were grown on Si (111) substrates by a Ga-assisted self-catalyzed method using molecular beam epitaxy. Before the growth, the substrates were first etched by hydrofluoric acid to partially remove the native oxide, followed by ultrasonication cleaning with ethanol and deionized water for 5 min each successively. After surface treatment, the GaAs NWs were grown with a duration of 150 min. During the NW synthesis, the substrate temperature was kept at 620 °C. The Ga beam equivalent pressure (BEP) was set as 6.2×10^{-8} Torr, while the V/III ratio was kept at 25.[24]

Preparation of GaAs 2DNLSs

The GaAs 2DNLSs were fabricated by using a chemical exfoliation method, as reported everywhere.[25,26] Firstly, GaAs (18 nm)/AlAs (50 nm) multiple quantum wells (MQWs) were grown on GaAs (111) substrates using molecular beam epitaxy. Then, the obtained MQWs were immersed in hydrofluoric acid to etch away the AlAs layers. In this case, the GaAs 2DNLSs would be dispersed in the solution. Lastly, the GaAs 2DNLSs were pulled out of the solution and transferred onto the p^+-Si substrate pre-grown with the 100 nm thick thermal oxide.

Fabrication of photodetectors

To start with the device fabrication, the GaAs NWs were mechanically exfoliated from the grown substrate and transferred onto the substrate pre-deposited with the GaAs 2DNLSs. After that, the Cr (15 nm)/Au (50 nm) electrodes were prepared onto the individual GaAs NW and GaAs sheet, respectively, by the standard procedures of electron beam lithography, metal evaporation and lift-off processes.

Characterization of materials and devices

The morphology of GaAs NWs was characterized by employing field-emission scanning electron microscopy (SEM) and transmission electron microscopy (TEM). The thickness of the GaAs 2DNLS was measured by using an atomic force microscope (AFM, Bruker Multimode 8). Raman spectroscopy of GaAs 2DNLSs was performed on a confocal microscope-based Raman spectrometer (WITec alpha 300) with a 532 nm laser. The current–voltage curves of the fabricated devices were measured with a standard probe station together with an Agilent 4155C semiconductor parameter analyzer. The corresponding time-dependent response curves were measured by coupling a pre-amplifier with an oscilloscope.

Results and discussion

As shown in the SEM image in Fig. S1,† the morphology of GaAs NWs is carefully investigated. It is observed that the typical NW has a diameter of ∼250 nm and a length of ∼10 μm. According to the TEM and selected area electron diffraction (SAED) image in Fig. 1(a), the GaAs NW has excellent crystallinity grown in the cubic zinc blende crystal structure, with a lattice spacing of 0.327 nm along the (111) planes. At the same time, the Raman spectrum of GaAs 2DNLSs is recorded and depicted in Fig. 1(c). Obviously, there is only one sharp peak located at 290.2 cm^{-1}, which is ascribed to the $A_1(LO)$ mode vibration of GaAs layers, indicating that the AlAs layers are fully removed with no impurity materials and phases here. The thickness of a representative GaAs 2DNLS is determined to be ∼18 nm by AFM as shown in the inset of Fig. 1(c), being consistent with the thickness of GaAs layers designed in the MQW structures. Combined with the clean surface obtained as evidenced in AFM, there is not any adverse effect induced by the material fabrication process for the synthesis of GaAs 2DNLS layers. After that, back-gate field-effect transistors (FETs) based on individual GaAs NWs and GaAs 2DNLSs are configured to evaluate their electrical properties accordingly. It is evident that both types of devices exhibit clear
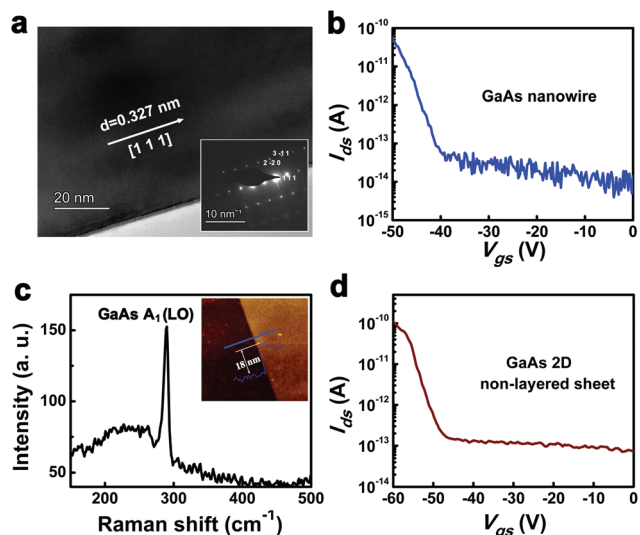
Fig. 1 (a) The high-resolution TEM image of the single GaAs NW. The inset is the SAED patterns of the GaAs NW taken along the [1 1 −2] zone axis. (b) Transfer characteristics (I_{ds}–V_{gs}) of a GaAs NW FET at V_{ds} = 1 V. (c) Raman spectrum of GaAs 2DNLSs. Inset shows the AFM image of a GaAs 2DNLS layer. (d) I_{ds}–V_{gs} curves of a GaAs 2DNLS FET at V_{ds} = 1 V.

p-type semiconducting characteristics. As presented in the device transfer curves in Fig. 1(b) and (d), the source–drain currents (I_{ds}) decrease with an increase in gate voltages (V_{gs}). All these results agree perfectly with the typical GaAs NWs and GaAs 2DNLSs obtained in the literature,[17,26] providing high-quality active materials for the subsequent device studies.

To shed light on the characteristics of surface states, the degrees of surface band bending of GaAs NWs and GaAs 2DNLSs are separately evaluated. The detailed output characteristics (I_{ds}–V_{ds} curves) of both types of devices are also given in ESI Fig. S2.† Along with the thermionic emission theory of the Schottky junction, the barrier height (φ_B) of the active device material can be calculated by using the following equations.[17,27,28]

$$J = J_S\left(\exp\left(\frac{qV}{nkT}\right) - 1\right) \quad (1)$$

$$q\varphi_B = \frac{kT}{q}\ln\left(\frac{A^*T^2}{J_S}\right) \quad (2)$$

where k is the Boltzmann constant, T is the temperature, V is the applied bias voltage, q is the electron charge, J_S is the saturation current density, A^* is the effective Richardson coefficient and n is the ideality factor. The value of A^* is known to be 74 A cm^{-2} K^{-2} for p-type GaAs.[29] The barrier heights of GaAs NWs and GaAs 2DNLSs can then be calculated from eqn (1) and (2). Notably, for GaAs, the band gap is 1.42 eV and the electron affinity energy is 4.07 eV, while the work function of Cr is 4.5 eV.[30,31] In this case, the degrees of band bending, presumably caused by the presence of surface states, are determined to be ~0.187 eV for GaAs NWs and ~0.201 eV for GaAs 2DNLSs (the detailed calculation process is shown in the ESI†). Although

the nanowire has a higher surface-to-volume ratio, the NW exhibits less band bending. It is attributed to the large surface states of 2DNLSs caused by chemical exfoliation. These band bending are quite significant compared with the band gap of the material.

Once the mixed-dimensional 1D–2D GaAs photodetector (*i.e.* GaAs NW/GaAs 2DNLS photodiode) is fabricated, the corresponding device schematic and optical image are illustrated in Fig. 2(a). It is clear that the junction length (*i.e.* the overlap length between the NW and the 2DNLS) of the device is ~700 nm. The energy band structure of the device is also calculated and depicted in Fig. 2(b). As expected, the GaAs NW and GaAs 2DNLS to have the same band gap and electron affinity except the different band bending, this would lead to a band offset at the interface (*i.e.* the overlap region). Owing to the bending down of the band gap for both NW and 2DNLS, a special band structure with an electron well and a hole barrier, being similar to a quasi-type-II structure, is resulted at the interface. In principle, the type-II structure is usually designed and implemented in the device design to further improve the separation efficiency of photo-generated carriers in the photodetector community.[32,33] Simultaneously, the electron well also provides a fast transport channel for electrons, which was established by accumulating electrons at the one-dimensional interface between the nanowire and 2D non-layer sheet. As a result, this special band structure is anticipated to contribute significant performance enhancement for optoelectronic devices.

To assess the device characteristics, I_{ds}–V_{ds} curves of the fabricated photodiode are measured in the dark and under illumination with a 532 nm laser as demonstrated in Fig. 2(c). The results are also presented in the semi-log plot of I_{ds} *versus*
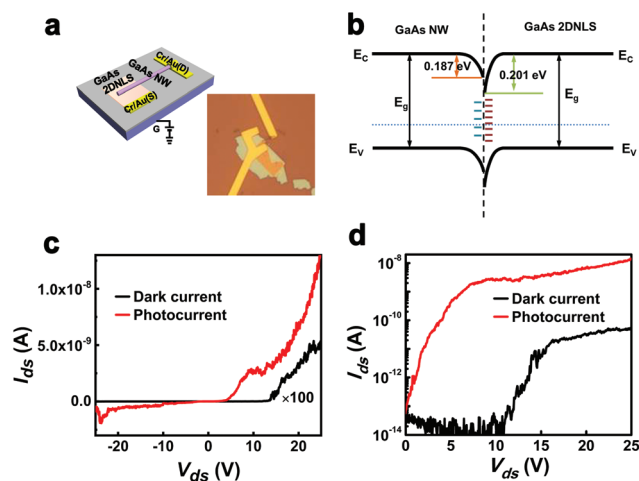

Fig. 2 (a) Schematic illustration of the mixed-dimensional GaAs NW/GaAs 2DNLS photodetector. The inset shows the optical image of the fabricated device. (b) Equilibrium band structure of the mixed-dimensional GaAs NW/GaAs 2DNLS photodetector. (c) I_{ds}–V_{ds} curves of the device measured in the dark and under illumination with a 532 nm laser. (d) The same results of panel c presented in the semi-log plot of I_{ds} *versus* V_{ds} at forward bias.

V_{ds} in Fig. 2(d). It is observed that the device shows a junction characteristic with a threshold voltage of ~5 V. Interestingly, when the voltage increases to ~10 V, the photocurrent increases slowly and starts to approach saturation. Once the voltage increases higher than 15 V, the dark current increases dramatically. This phenomenon is attributed to the special band structure caused by the interface states. If a 5 V bias is applied to the device, the conduction band of the GaAs NW is flattened. Then, the electrons in both GaAs NW and 2DNLS are able to transport on the conduction band. Therefore, the forward conduction of the photodiode is resulted. However, there is a valence band barrier existing at the interface, leading to the accumulation of holes on the GaAs NW side. In this case, even though the voltage increases further, the current would approach saturation. When the voltage hits to a value of 15 V, the holes in the GaAs NW start to overpass the barrier and transport to the GaAs 2DNLS. For this reason, the dark current increases substantially to yield the above-mentioned phenomenon. The corresponding band diagrams of the mixed-dimensional GaAs photodetector operated at various voltages are illustrated in Fig. S4.†

In addition, the I_{ds}–V_{ds} curves of the photodetector are also investigated with different illumination power density as shown in Fig. 3(a). Evidently, the photocurrent is observed to increase with the increasing power density. It is also noted that all the curves exhibit the double-threshold characteristics. Furthermore, responsivity (R) and detectivity (D^*), the two key figure-of-merits of photodetectors, are employed to evaluate the device performance here. These two parameters can be calculated by using the following equations.[29]

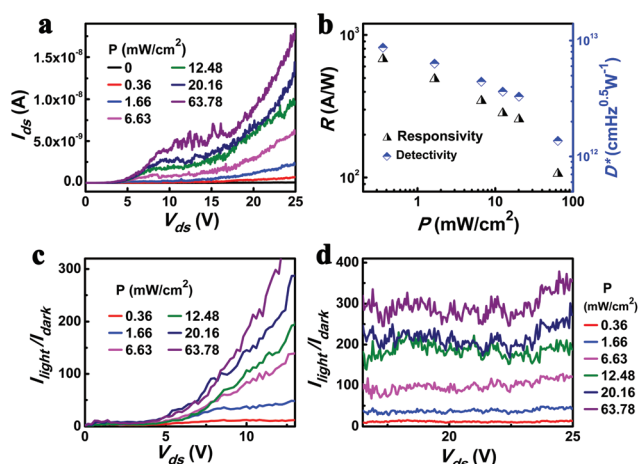$$R = \frac{I_{light} - I_{dark}}{PS} \quad (3)$$

Fig. 3 (a) I_{ds}–V_{ds} curves of the mixed-dimensional GaAs NW/GaAs 2DNLS photodetector with different laser power densities. (b) Dependences of R and D^* of the photodetector with different laser power intensities. (c and d) The ratio of photocurrent to dark current with the bias voltage range of 0–13 V and 16–25 V at various laser power intensities, respectively.

$$D^* = \frac{R}{\sqrt{2qI_{dark}/S}} \quad (4)$$

where I_{light} is the photocurrent, I_{dark} is the dark current, P is the laser power density, S is the effective area of the photosensitive region and q is the electron charge. This way, the values of responsivity and detectivity can be determined at various power densities at 25 V and compiled in Fig. 3(b). The maximum responsivity and detectivity are found to be 667 A W^{-1} and 8.69×10^{12} cm $Hz^{0.5}$ W^{-1}, respectively. In fact, the responsivity and detectivity values would decrease with the increasing laser power density, which can be explained by the competition between photo-generated electron–hole pair recombination and separation. At low power density, the enhanced carrier separation rate results in higher responsivity, while at high power density, responsivity is reduced due to the increased carrier recombination rate.[24] At the same time, to reveal the physical mechanism taking place at the NW/2DNLS interface, individual GaAs NW photodetectors and GaAs 2DNLS photodetectors are fabricated and studied to serve as the control references. It is seen that the R value of the single GaAs NW photodetector is found to be 2.15 A W^{-1} at a bias voltage of 5 V and a laser power density of 19.52 mW cm^{-2}, whereas the R value of the GaAs 2DNLS photodetector is determined to be 15.76 mA W^{-1} at the same bias voltage and a laser power density of 20.16 mW cm^{-2} (ESI Fig. S5†). These responsivity results are a lot smaller than that (8.75 A W^{-1}) of the mixed-dimensional GaAs NW/GaAs 2DNLS photodetector at the similar conditions. As compared with the state-of-the-art low-dimensional GaAs based photodetectors, our developed mixed-dimensional GaAs device has already delivered the substantial enhancement in all of the performance parameters (Table 1). It is believed that this performance improvement is attributed to the formation of a quasi-type-II band structure and electron well as discussed above. The quasi-type-II band structure promotes the photo-generated carrier separation and reduces the carrier recombination efficiency. The electron well provides a high-speed channel for photo-generated electrons, where their carrier separation speed can be accelerated. Hence, the responsivity of the mixed-dimensional photodetector is greatly enhanced. The ratios of photocurrent to dark current (I_{light}/I_{dark}) before and after the second threshold are also measured and presented in Fig. 3(c) and (d). It is clearly observed that the I_{light}/I_{dark} ratio increases with the increasing laser power density, which is ascribed to the higher laser power density providing more photo-generated carriers. Moreover, the I_{light}/I_{dark} ratio also increases with the increasing bias voltage in the range from 0 to 13 V since more carriers can be extracted from the interface states at higher bias voltage. Nevertheless, the I_{light}/I_{dark} ratio remains pretty steady in the higher bias voltage range from 16 to 25 V. At high bias voltage, the band bending at the interface is reduced and the barriers are more or less eliminated. In this case, the carriers trapped at the interface region would get depleted and hence the photo-generated carriers become fully separated. As a result, the I_{light}/I_{dark} ratios do not exhibit any changes with the

Table 1 Comparison of the performance parameters of our mixed-dimensional GaAs devices with other state-of-the-art low-dimensional GaAs based photodetectors

Device structure	Wavelength (nm)	Responsivity (mA W^{-1})	Detectivity (cm Hz$^{0.5}$ W^{-1})	Ref.
GaAs/AlGaAs core–shell NW	855	570 (2 V)	7.2×10^{10}	34
GaAs NW/graphene	532	351.2 (0 V)	7.2×10^{9}	35
GaAs NW/graphene	532	231 (0 V)	1.6×10^{9}	36
GaAs nanocone/graphene	850	1.73 (0 V)	1.83×10^{11}	37
UCNPs/GaAs NW/graphene^a	980	5.97 (0 V)	1.1×10^{11}	38
GaAs NW	532	2.5×10^4 (1 V)	9.04×10^{12}	17
GaAs NW	532	1.175×10^6 (1 V)	9.52×10^{11}	27
GaAs NW	300–1500	1.2 (2 V)	—	39
GaAs NW/GaAs 2DNLS	532	6.77×10^5 (25 V)	8.69×10^{12}	This work

^{a} UCNPs, up-conversion nanoparticles.

increasing bias voltage (*i.e.* from 16 to 25 V). All these results demonstrate the photoresponse improvement of the mixed-dimensional GaAs device as contrasted with the conventional photodetectors.

Apart from the steady-state photoresponse, the time-dependent characteristics of the mixed-dimensional GaAs photodiode are examined under illumination with a 532 nm laser at V_{ds} = 8 V and 15 V, respectively. The normalized time-dependent current curves are then shown in Fig. 4(a) and (b), correspondingly. It is clear that the device exhibits the stable and reproducible on–off switching response. At 8 V, when the laser turns on and off, the photocurrent rises up and drops down abruptly. The rise time is referred to the time interval required for the photocurrent to increase from 10 to 90% of its peak value, while the decay time is from 90 to 10% of the peak value. The rise time and decay time are found to be 8 ms and 6 ms, respectively. At the same time, the rise time and decay time of the single GaAs NW photodetector are found to be 70 ms and 52 ms, whereas these values of the GaAs 2DNLS photodetector are determined to be 300 ms and 270 ms (ESI

Fig. S6†), which are much higher than the GaAs NW/GaAs 2DNLS photodetector. However, when the bias is increased to 15 V, the photocurrent would show a "double-rise" feature, with a first slow rise time of 8 ms followed by a second fast rise time of 90 ms, under illumination (the high-resolution current *versus* time curves to illustrate the rise and decay times are shown in ESI Fig. S7†). This unique feature can be attributed to the difference of band bending existing at the NW/2DNLS interface. The band structures of the NW/2DNLS region at 8 V and 15 V are shown in Fig. 4(c) and (d), respectively. When a bias of 8 V is applied, the device current mainly comes from the electron transport along the conduction band of GaAs NW together with the hole transport along the valence band of GaAs 2DNLS. Once a bias of 15 V is applied, the hole current does not only originate from the GaAs 2DNLS but also comes from the GaAs NW. Owing to the interface barrier, there would be an accumulation of holes, which leads to the double-rise feature observed in the on–off switching photoresponse. In any case, the reversible photoswitching characteristics clearly indicate the excellent stability and photosensing capability of mixed-dimensional GaAs devices.

Besides, it is well known that the surface states of semiconductors can be strongly affected by ambient conditions,[40] but the interface states are insensitive to the changes of ambient environments. In order to evaluate the effect of different ambient environments on the photoresponse properties of the mixed-dimensional GaAs device, the I_{ds}–V_{ds} curves at various power density and time-dependent photoresponse measurements under different ambient conditions are carried out. As depicted in Fig. 5a and b, it is observed that the I_{ds}–V_{ds} curves of the devices exhibit a similar behavior between Ar and O_2. The curves illustrate the double-threshold characteristics, which agree well with the results discussed in Fig. 3a. Also, the high-resolution current–time curves demonstrate the on–off switching photoresponse at a bias of 8 V and the "double-rise" phenomenon at a bias of 15 V as given in Fig. 3c and d, respectively, being perfectly consistent with the observation in Fig. 4. More importantly, the rise time and decay time of the device are found to be the same with the measurement performed under Ar, O_2 and vacuum conditions at different respective bias voltages. All these results evidently reveal that the interface states established with NW and
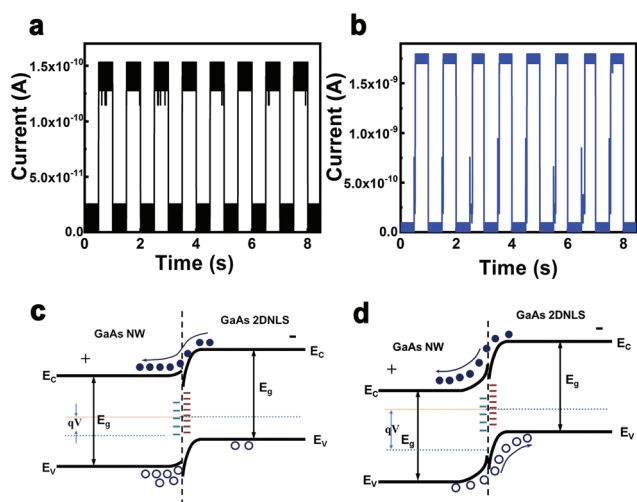

Fig. 4 Time-dependent photoresponses of the mixed-dimensional GaAs NW/GaAs 2DNLS photodetector operated at a bias of (a) 8 V and (b) 15 V. The corresponding band structures of the mixed-dimensional GaAs photodetector operated at (c) 8 V and (d) 15 V.
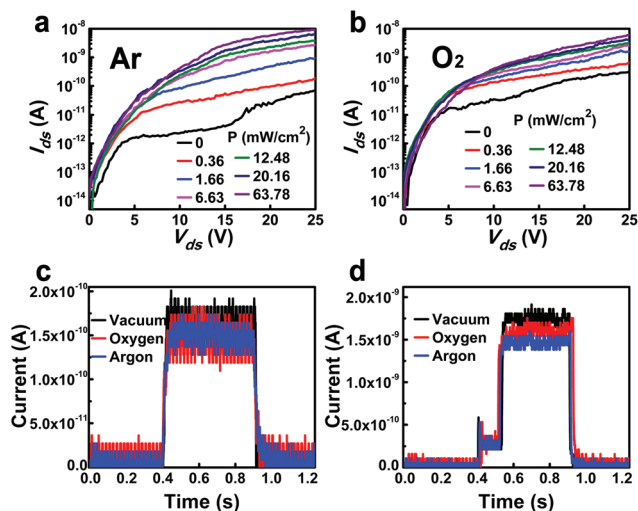
Fig. 5 I_{ds}–V_{ds} curves of the mixed-dimensional GaAs NW/GaAs 2DNLS photodetector measured with different laser power densities in (a) argon and (b) oxygen. High-resolution time-dependent photoresponse of the mixed-dimensional photodetector in different ambient environments operated at a bias of (c) 8 V and (d) 15 V.

2DNLS are independent of ambient environments, pointing out the stable performance of the device.

Conclusions

In summary, we design and fabricate the high-performance mixed-dimensional GaAs NW/GaAs 2DNLS photodetectors. In this device structure, there is a unique utilization of the constructive interface states established by the harmful surface states of the GaAs NW and the GaAs 2DNLS. Detailed experimental studies are put forward to investigate the effects of these surface states and interface states on the photoresponse characteristics of fabricated devices. It is impressive that the mixed-dimensional GaAs photodetector exhibits a responsivity of 677 A W^{-1} and a detectivity of 8.69 × 10^{12} cm Hz$^{0.5}$ W^{-1}, which are already much higher than those of state-of-the-art low-dimensional GaAs photodetectors. These results do not only pave an effective way to utilize the surface states by putting up constructive interface states of the device materials, but also demonstrate the superior advantages of these interface states for the further performance enhancement of mixed-dimensional GaAs photodetectors.

Conflicts of interest

There are no conflicts to declare.

Acknowledgements

Notes and references

1 L. Britnell, R. V. Gorbachev, R. Jalil, B. D. Belle, F. Schedin, M. I. Katsnelson, L. Eaves, S. V. Morozov, A. S. Mayorov, N. M. R. Peres, A. H. C. Neto, J. Leist, A. K. Geim, L. A. Ponomarenko and K. S. Novoselov, *Nano Lett.*, 2012, **12**, 1707–1710.

2 F. Withers, O. Del Pozo-Zamudio, A. Mishchenko, A. P. Rooney, A. Gholinia, K. Watanabe, T. Taniguchi, S. J. Haigh, A. K. Geim, A. I. Tartakovskii and K. S. Novoselov, *Nat. Mater.*, 2015, **14**, 301–306.

3 K. S. Novoselov, A. Mishchenko, A. Carvalho and A. H. Castro Neto, *Science*, 2016, **353**, aac9439.

4 J. Chen, Z. Li, F. Ni, W. Ouyang and X. Fang, *Mater. Horiz.*, 2020, **7**, 1828–1833.

5 Z. Zou, D. Li, J. Liang, X. Zhang, H. Liu, C. Zhu, X. Yang, L. Li, B. Zheng, X. Sun, Z. Zeng, J. Yi, X. Zhuang, X. Wang and A. Pan, *Nanoscale*, 2020, **12**, 6480–6488.

6 Y. T. Lee, P. J. Jeon, J. H. Han, J. Ahn, H. S. Lee, J. Y. Lim, W. K. Choi, J. D. Song, M. C. Park, S. Im and D. K. Hwang, *Adv. Funct. Mater.*, 2017, **27**, 1703822.

7 L. Liao, Y. C. Lin, M. Bao, R. Cheng, J. Bai, Y. Liu, Y. Qu, K. L. Wang, Y. Huang and X. Duan, *Nature*, 2010, **467**, 305–308.

8 X. Xu, J. Chen, S. Cai, Z. Long, Y. Zhang, L. Su, S. He, C. Tang, P. Liu, H. Peng and X. Fang, *Adv. Mater.*, 2018, **30**, 1803165.

9 L. Zhuo, P. Fan, S. Zhang, X. Liu, X. Guo, Y. Zhang, Y. Zhan, D. Li, Z. Che, W. Zhu, H. Zheng, J. Tang, J. Zhang, Y. Zhong, Y. Luo, J. Yu and Z. Chen, *Nanoscale*, 2020, **12**, 14188–14193.

10 G. Konstantatos, M. Badioli, L. Gaudreau, J. Osmond, M. Bernechea, F. P. G. de Arquer, F. Gatti and F. H. Koppens, *Nat. Nanotechnol.*, 2012, **7**, 363–368.

11 D. Jariwala, T. J. Marks and M. C. Hersam, *Nat. Mater.*, 2017, **16**, 170–181.

12 Y. Liu, N. O. Weiss, X. Duan, H. C. Cheng, Y. Huang and X. Duan, *Nat. Rev. Mater.*, 2016, **1**, 16042.

13 Z. Zhang, P. Lin, Q. Liao, Z. Kang, H. Si and Y. Zhang, *Adv. Mater.*, 2019, **31**, 1806411.

14 K. Fichthorn, *Nat. Mater.*, 2019, **18**, 911–912.

15 S. Liu, L. Xie, H. Qian, G. Y. Liu, H. Zhong and H. B. Zeng, *J. Mater. Chem. A*, 2019, **7**, 15411–15419.

16 J. Yang, Z. Zeng, J. Kang, S. Betzler, C. Czarnik, X. Zhang, C. Ophus, C. Yu, K. Bustillo, M. Pan, J. Qiu, L. W. Wang and H. Zheng, *Nat. Mater.*, 2019, **18**, 970–976.

17 X. Chen, N. Xia, Z. Yang, F. Gong, Z. Wei, D. Wang, J. Tang, X. Fang, D. Fang and L. Liao, *Nanotechnology*, 2018, **29**, 095201.

18 X. Liu, Z. Wei, J. Liu, W. Tan, X. Fang, D. Fang, X. Wang, D. Wang, J. Tang and X. Fan, *Appl. Surf. Sci.*, 2018, **436**, 460–466.

19 K. Zhang, Y. Wei, J. Zhang, H. Ma, X. Yang, G. Lu, K. Zhang, Q. Li, K. Jiang and S. Fan, *Proc. Natl. Acad. Sci. U. S. A.*, 2019, **116**, 6586–6593.

20 A. Bera and D. Basak, *Appl. Phys. Lett.*, 2008, **93**, 053102.

21 M. M. Fan, K. W. Liu, X. Chen, X. Wang, Z. Z. Zhang, B. H. Li and D. Z. Shen, *ACS Appl. Mater. Interfaces*, 2015, **7**, 20600–20606.

22 A. Dong, Z. Pei, J. Yuan, S. Qian, J. Tao and H. Wang, *Nanotechnology*, 2019, **30**, 375705.

23 H. Tian, A. Hu, Q. Liu, X. He and X. Guo, *Adv. Opt. Mater.*, 2020, **8**, 1901741.

24 Y. Kang, J. Tang, P. Wang, F. Lin, X. Fang, D. Fang, D. Wang, X. Wang and Z. Wei, *Mater. Res. Express*, 2018, **6**, 035012.

25 P. C. Tao, S. Yao, F. Y. Liu, B. Wang, F. Huang and M. Y. Wang, *J. Mater. Chem. A*, 2019, **7**, 23512–23536.

26 J. Yoon, S. Jo, I. S. Chun, I. Jung, H. S. Kim, M. Meitl, E. Menard, X. Li, J. J. Coleman, U. Paik and J. A. Rogers, *Nature*, 2010, **465**, 329–333.

27 J. Bardeen, *Phys. Rev.*, 1947, **71**, 717.

28 A. M. Cowley and S. M. Sze, *J. Appl. Phys.*, 1965, **36**, 3212.

29 X. Chen, D. Wang, T. Wang, Z. Yang, X. Zou, P. Wang, W. Luo, Q. Li, L. Liao, W. Hu and Z. Wei, *ACS Appl. Mater. Interfaces*, 2019, **11**, 33188–33193.

30 Z. J. Xu, S. S. Lin, X. Q. Li, S. J. Zhang, Z. Q. Wu, W. L. Xu, Y. H. Lu and S. Xu, *Nano Energy*, 2016, **23**, 89–96.

31 H. Ali, Y. Zhang, J. Tang, K. Peng, S. Sun, Y. Sun, F. Song, A. Falak, S. Wu, C. Qian, M. Wang, Z. Zuo, K. J. Jin, A. M. Sanchez, H. Liu and X. Xu, *Small*, 2018, **14**, e1704429.

32 L. H. Zeng, S. H. Lin, Z. J. Li, Z. X. Zhang, T. F. Zhang, C. Xie, C. H. Mak, Y. Chai, S. P. Lau, L. B. Luo and Y. H. Tsang, *Adv. Funct. Mater.*, 2018, **28**, 1705970.

33 L. Wang, J. S. Jie, Z. B. Shao, Q. Zhang, X. H. Zhang, Y. M. Wang, Z. Sun and S. T. Lee, *Adv. Funct. Mater.*, 2015, **25**, 2910–2919.

34 X. Dai, S. Zhang, Z. L. Wang, G. Adamo, H. Liu, Y. Z. Huang, C. Couteau and C. Soci, *Nano Lett.*, 2014, **14**, 2688–2693.

35 Y. Luo, X. Yan, W. Wei, M. Zhang, J. Zhang, B. Li, J. Zheng, Q. Lu, Q. Lin, W. Liu, X. Zhang and X. Ren, *J. Vac. Sci. Technol., B: Nanotechnol. Microelectron.: Mater., Process., Meas., Phenom.*, 2018, **36**, 051205.

36 Y. Luo, X. Yan, J. Zhang, B. Li, Y. Wu, Q. Lu, C. Jin, X. Zhang and X. Ren, *Nanoscale*, 2018, **10**, 9212–9217.

37 L. B. Luo, J. J. Chen, M. Z. Wang, H. Hu, C. Y. Wu, Q. Li, L. Wang, J. A. Huang and F. X. Liang, *Adv. Funct. Mater.*, 2014, **24**, 2794–2800.

38 J. Wu, Z. Yang, C. Qiu, Y. Zhang, Z. Wu, J. Yang, Y. Lu, J. Li, D. Yang, R. Hao, E. Li, G. Yu and S. Lin, *Nanoscale*, 2018, **10**, 8023–8030.

39 C. G. Nunez, A. F. Brana, N. Lopez, J. L. Pau and B. J. Garcia, *Nanotechnology*, 2020, **31**, 225604.

40 M. M. Fan, K. W. Liu, Z. Z. Zhang, B. H. Li, X. Chen, D. X. Zhao, C. X. Shan and D. Z. Shen, *Appl. Phys. Lett.*, 2014, **105**, 011117.